Supplementary Information for

Molecular-scale investigation of Cu(II) interactions with synthetic and natural zeolites during removal and recovery

Case M. van Genuchten[1]*, *Kaifeng Wang*[1], *Claus Kjøller*[1], *Knud Dideriksen*[1]

[1]Department of Geochemistry, Geological Survey of Denmark and Greenland (GEUS), Øster Voldgade 10, Copenhagen, Denmark

Corresponding Author: cvg@geus.dk

Pages: 22

Figures: 10

Tables: 4

S1. PHREEQC model and fitting of isotherm data

The PHREEQC model was intended to allow simulations at both lower and higher salinity. Consequently, we based the model on the Pitzer approach for calculation of activity coefficients, using the geodat_1-4 database by Moog and Cannepin (2014) as a starting point. This database has been developed for use in geothermal systems. However, it does not have Pitzer parameters for Cu. As the first step of the modelling, we therefore tested the performance of several Pitzer parameter datasets for the Cu-Na-Cl-H_2O system in combination with the geodat_1-4 database (Downes and Pitzer, 1976; Kim and Frederick, 1988; Haung, 1989; Ma et al., 2019). The Haung, 1989 dataset performed the best, albeit with some mismatch compared to the speciation provided in the corresponding publication. To match the speciation, various alterations to the thermodynamic dataset were tested. After slight adjustments by omitting the $CuCl^+$-Cl^- interaction and changing the value for the stability of the $CuCl_4^{2-}$ complex, the simulations with the parameter set provided by Haung (1989), shown in Figure S2A, yielded reasonable agreement with the aqueous speciation given in the publication. In addition, simulated results agree with the solubility determined for atacamite (Le Roux et al., 2016; Figure S2B), the least soluble phase in our experimental conditions. Thus, this thermodynamic model allowed simulation with tolerable accuracy of published experimental and theoretical results. However, it is limited to 25 °C. The parameters of the thermodynamic model are given in Tables S1 and S2.

Using this thermodynamic model, we fitted model parameters to adsorption isotherms measured at room temperature. The datasets included in the fitting were Cu(II) adsorption to synthetic faujasite at pH 5 and 6 and to natural clinoptilolite at pH 5 (the pH 6 data was omitted to the predominance of Cu-Cu polymerization). In the fitting, we optimised the values for the stability constant for the exchange reaction as well as the cation exchange capacity (CEC). The exchange reactions are given by:

$2\ NaX + Cu^{2+} = CuX_2 + 2\ Na^+$,

with a stability constant, K_{Me} given by:

$$K_{Me} = \frac{(NaX)^2(Cu^{2+})}{(Na^+)^2(CuX_2)} \quad \text{(Eq. S1)}$$

Here, X represents an exchange site with a concentration dictated by the CEC; (Na^+) and (Cu^{2+}), the activity of aqueous Na^+ and Cu^{2+}; and (NaX) and (CuX_2), the activity of the ions in the zeolite, which were calculated based on equivalent fractions (the Gaines-Thomas convention).

To assess uncertainties in the fitting, we used two types of software, PHREEPLOT and our own custom-made python routine (Vital et al., 2025), both of which were used to fit the systems element wise. For the python-based fitting, we also fitted the adsorption data for both elements simultaneously (i.e., with a single value for CEC for each zeolite). For all optimisation of the equilibrium constants and CEC, we minimised the sum of the squared residuals between the measured and calculated values for both the aqueous concentrations and the amount taken up. Given that the fitting is based on absolute differences, it would provide a better fit of the experimental data at higher Me concentrations, which we expect would be important when CEC is also fitted.

S2. Synchrotron X-ray diffraction measurements of Cu(II)-loaded zeolites at the European Synchrotron Radiation Facility.

Complementary XRD data for a subset of Cu(II)-loaded zeolite samples was obtained to identify structural changes that had occurred in response to Cu(II) exposure. The data were collected at Beamline ID31 of the European Synchrotron Radiation Facility (ESRF). For the measurements, powdered samples were loaded into ~1 mm thick, cylindrical slots that were mounted between Kapton windows in a sample holder. The measurement was conducted in

transmission geometry with an X-ray energy of 75.05 keV. The intensities of scattered X-rays were measured with a Pilatus CdTe 2M detector (1679 x 1475 pixels with pixel size of 172 x 172 μm^2) positioned such that the incoming beam was located at the detector corner and that sample-to-detector distance was approximately 30 cm. The geometry of the setup was calibrated with LaB6 (NIST SRM 660b) and the software pyFAI.[22] Data are reported with the x-axis in Q-space.

S3. Shell-by-shell fitting procedure for endmember EXAFS spectra

Phase and amplitude functions for single- and multiple-scattering (MS) paths were calculated using FEFF6 (Rehr et al., 1992), and included Cu-O, Cu-Cu and Cu-O-O derived from the structure of spertiniite (Oswald et al., 1990) and Cu-Si/Al derived from the structure of dioptase (Belokoneva et al., 2002). Theoretical curve fits were based on algorithms derived from IFEFFIT (Newville, 2001) and were performed from 1 to 4 Å in R+ΔR-space. Parameters varied in the fits typically included the interatomic distance (R), the coordination number (CN) and the change in threshold energy (ΔE_0). However, due to high fit-derived correlations between CN and σ^2, particularly for second-shell fits, we constrained σ^2 for Cu-Cu (0.006-0.007 Å^2) and Cu-Si/Al (0.012 Å^2) atomic pairs to values reported for previous fits of CuO (Cheah et al., 2000) and Cu(II) sorbed to faujasite (Sushkevich et al., 2020), respectively. In addition, despite the expected distortion of first-shell oxygen atoms for Cu(II) polyhedra, we followed the fitting approach of Cheah et al., 2000 and included a Cu-O-O MS path with CN and σ^2 constrained to 8 and 0.007 Å^2 respectively, which reflects MS from first-shell equatorial oxygen atoms (Cheah et al., 2000). We note here that the fitting routine cannot distinguish between backscattering from Cu-Si and Cu-Al atoms due to the similar atomic number of Si and Al. Therefore, we report fitting results involving Si and Al as Cu-Si/Al (Sushkevich et al., 2020). The goodness-of-fit was evaluated using the R-factor, which is the mean square

difference between the fit and the data on a point-by-point basis: $R = \sum_i (data_i - fit_i)^2 / \sum_i (data_i)^2$.

S4. Synchrotron X-ray diffraction results for Cu(II)-loaded zeolites

After exposure to 3 mM Cu(II), patterns for both the synthetic faujasite and natural clinoptilolite displayed increased diffraction intensity at positions where atacamite ($Cu_2(OH)_3Cl$) peaks are expected (1.15, 2.22, 2,28, 2.77, 3.45 and 3.66 Å). These are sometimes visible as proper peaks or shoulders in the measured data (Figure S8), but are clear in the calculated patterns of the difference between reacted and unreacted solids (grey lines in Figure S8). For the calculated difference patterns, small peaks for atacamite are also discernible for the data obtained with 0.6 mM Cu at pH 6. For all samples plotted in Figure S8, the solutions are predicted to be supersaturated with respect to atacamite using PHREEQC, implying favorable thermodynamics for its formation. Thus, we conclude that atacamite formed in at least some of the experiments where aqueous Cu(II) concentration exceeded its solubility, which was particularly the case for the pH 6 samples containing the highest polymeric Cu(II) content derived by EXAFS analysis.

S5. Results of faujasite adsorption modelling

For the faujasite sample series, a larger adsorption dataset is available that appears to consist of primarily monomeric Cu adsorption (Figure 5 in the main text), which allowed us to fit constants for a cation exchange model and test its applicability using the adsorption experiments at variable NaCl concentrations (Figure 3 in the main text). These results are shown in Figure S10 and the derived constants and CEC are shown in Table S4. In general, the calculated values agree reasonably well with those measured and the parameters fitted with the two methods are consistent. One key finding relevant here is that our models of the adsorption

118 data, which fit reasonably well, did not consider differences in monomeric Cu(II) binding that
119 were revealed in the EXAFS analysis (*i.e.,* outer-sphere and inner-sphere). For the faujasite
120 samples, the EXAFS analysis did not indicate a systematic relationship between the occurrence
121 of either of the two monomeric Cu species with Cu(II) loading, pH or time. This lack of
122 systematic trend suggests that the stability of the two types of monomeric Cu coordination
123 environments might be quite similar, such that minute differences in experimental conditions
124 or sample preparation might cause shifts in their relative abundance. Therefore, pooling the
125 two species during modelling makes sense because it decreases the number of adjustable
126 parameters and it does not introduce substantial error in the fitting.
127
128

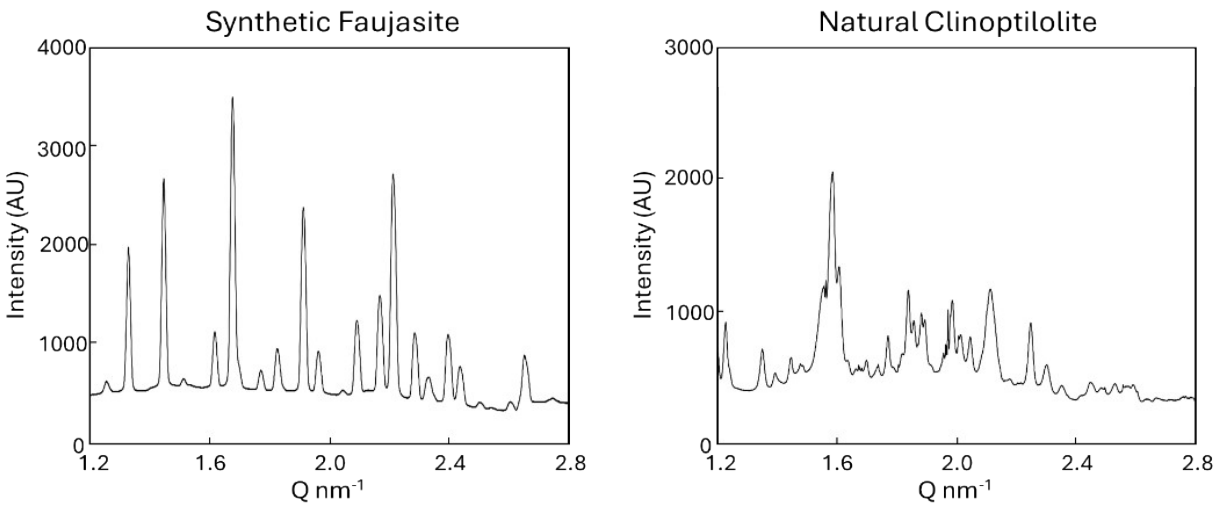

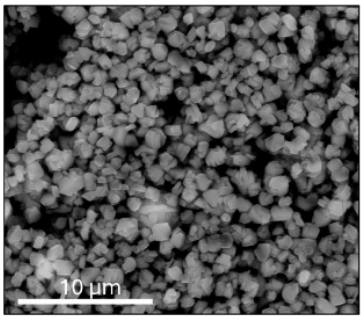

Element	Mass Fraction (%) EDS of 9 Points
C	**0 ± 0**
Si	26.7 ± 1.1
Al	11.5 ± 0.4
Na	8.5 ± 0.6
O	49.8 ± 1.3

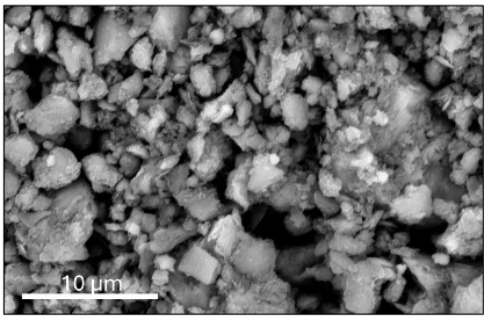

Element	Mass Fraction (%) EDS of 9 Points
C	**3.8 ± 0.8**
Si	31.5 ± 1.8
Al	5.6 ± 1.1
Na	2.4 ± 0.7
O	53.3 ± 1.5

Figure S1: Structural data for the initial zeolite samples. Data for synthetic faujasite and natural clinoptilolite are presented on the left and right sides, respectively. Synchrotron X-ray diffraction data is presented in the top panels, whereas SEM-EDS data are presented in the middle and bottom panels. The elemental composition given in this figure represents an average of nine points for which EDS data were obtained. Notably, the synthetic faujasite sample has substantially less C, implying less impurities in the solids than the natural clinoptilolite sample.

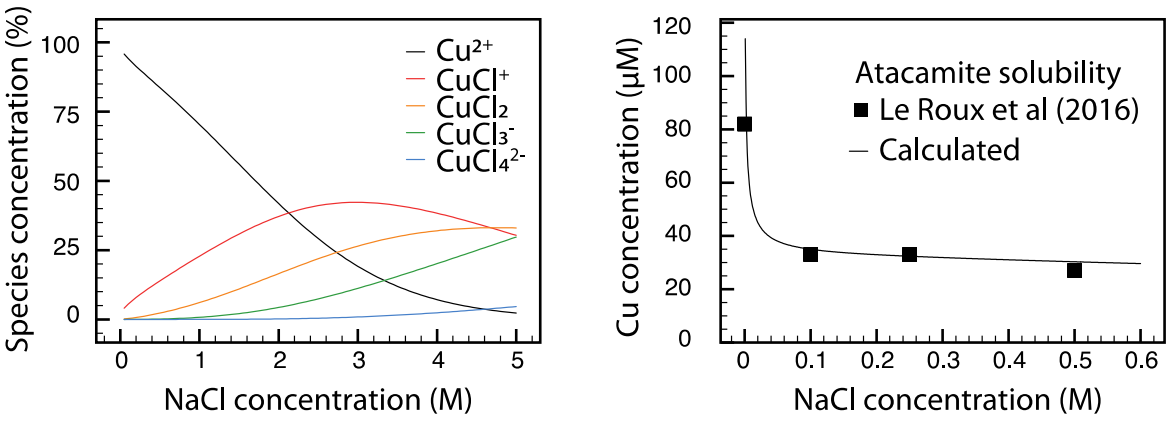

Figure S2. A) Calculated Cu(II) speciation with the Pitzer model used. B) Calculated and measured solubility of atacamite.

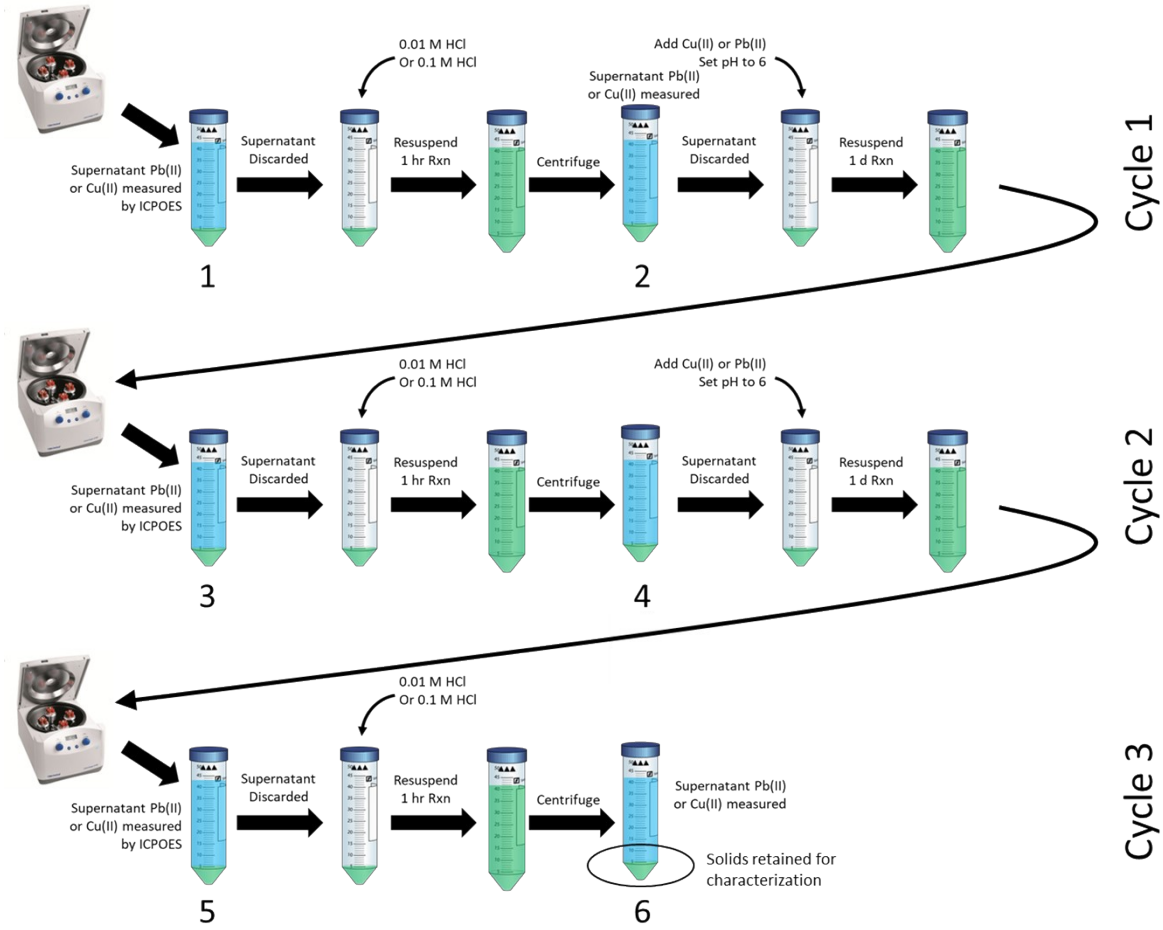

143

144 Figure S3: Schematic of the regeneration experimental protocol. In this schematic, numbers
145 1-6 represent the following: 1) Initial adsorption experiment, 2) Cu(II) loading after the first
146 acidic regeneration, 3) Cu(II) loading after the second adsorption experiment, 4) Cu(II) loading
147 after the second acidic regeneration, 5) Cu(II) loading after the final adsorption experiment, 6)
148 Cu(II) loading after the final acidic regeneration. The solids obtained after the final
149 regeneration experiment were retained for synchrotron-based analysis.

150

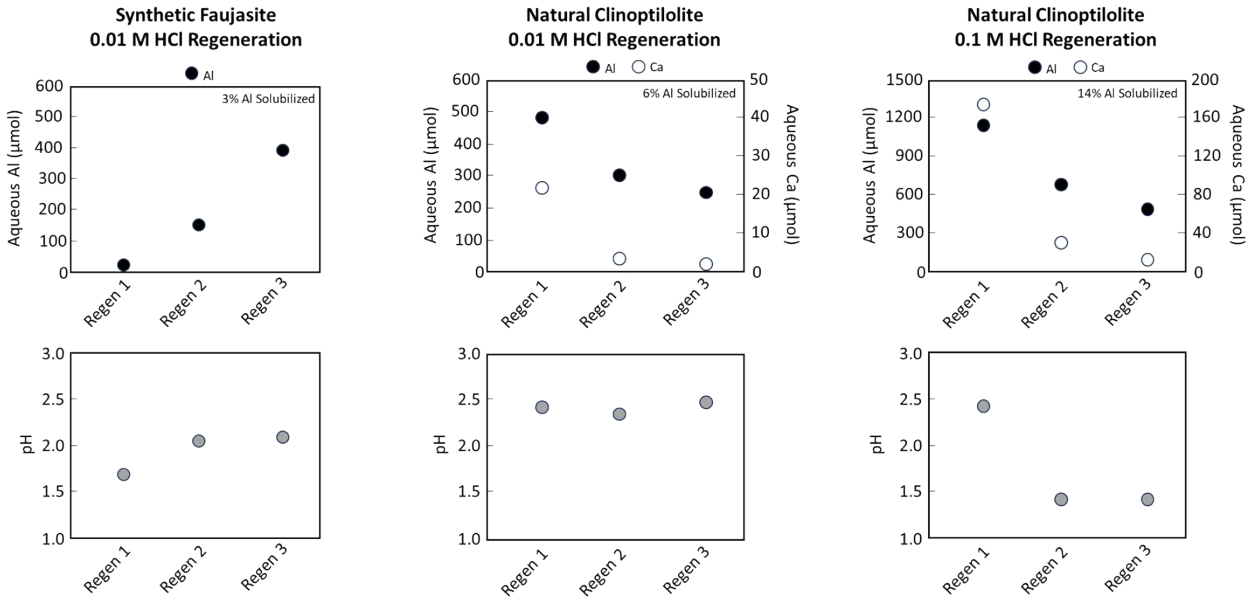

Figure S4: Solution composition following repeated cycles of acidic regeneration for synthetic faujasite using 0.01 M HCl (left panels) and natural clinoptilolite using 0.01 M HCl (middle panels) and 0.1 M HCl (right panels). The release of Al (black symbols) and Ca (white symbols) are plotted on the top panels, whereas pH is given in the bottom panels. Note that Ca was not released from the synthetic faujasite sample because Ca is not present in this solid. The initial solids content for each sample was 5 g/L.

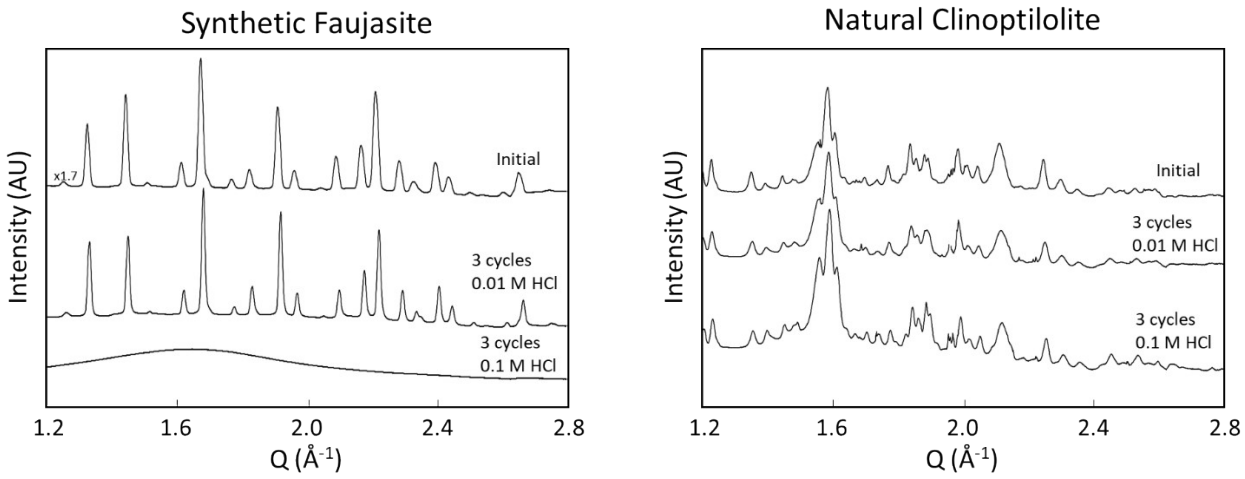

159

160 Figure S5: Synchrotron XRD of synthetic faujasite (left) and natural clinoptilolite (right)
161 following repeated cycles of acidic regeneration using 0.01 M and 0.1 M HCl. The solids
162 remaining after three cycles of 0.1 M HCl regeneration of the faujasite samples resembled a
163 gel and no Bragg diffraction peaks were observed in the XRD pattern, consistent with the
164 disintegration of the faujasite crystal in highly acidic conditions.

165

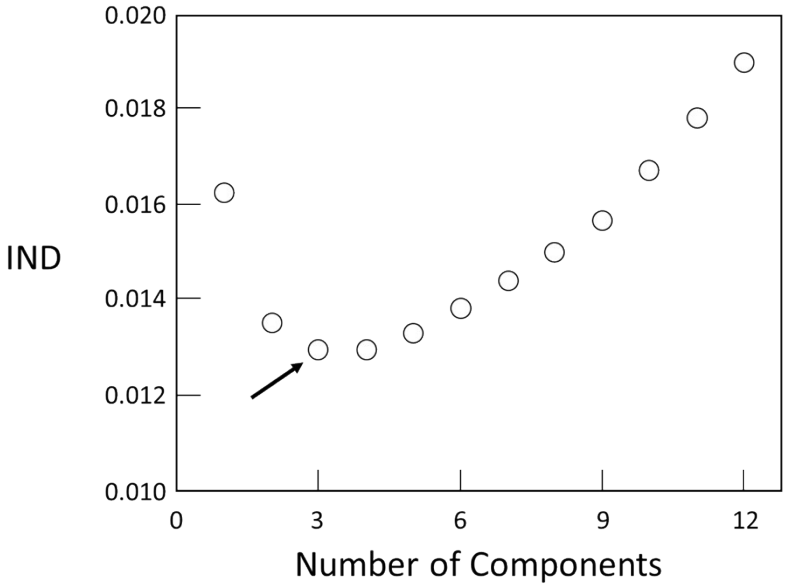

Figure S6: Results of the principal component analysis. IND is plotted as a function of the number of independent components. The arrow highlights the minimum of the IND function when three components are used.

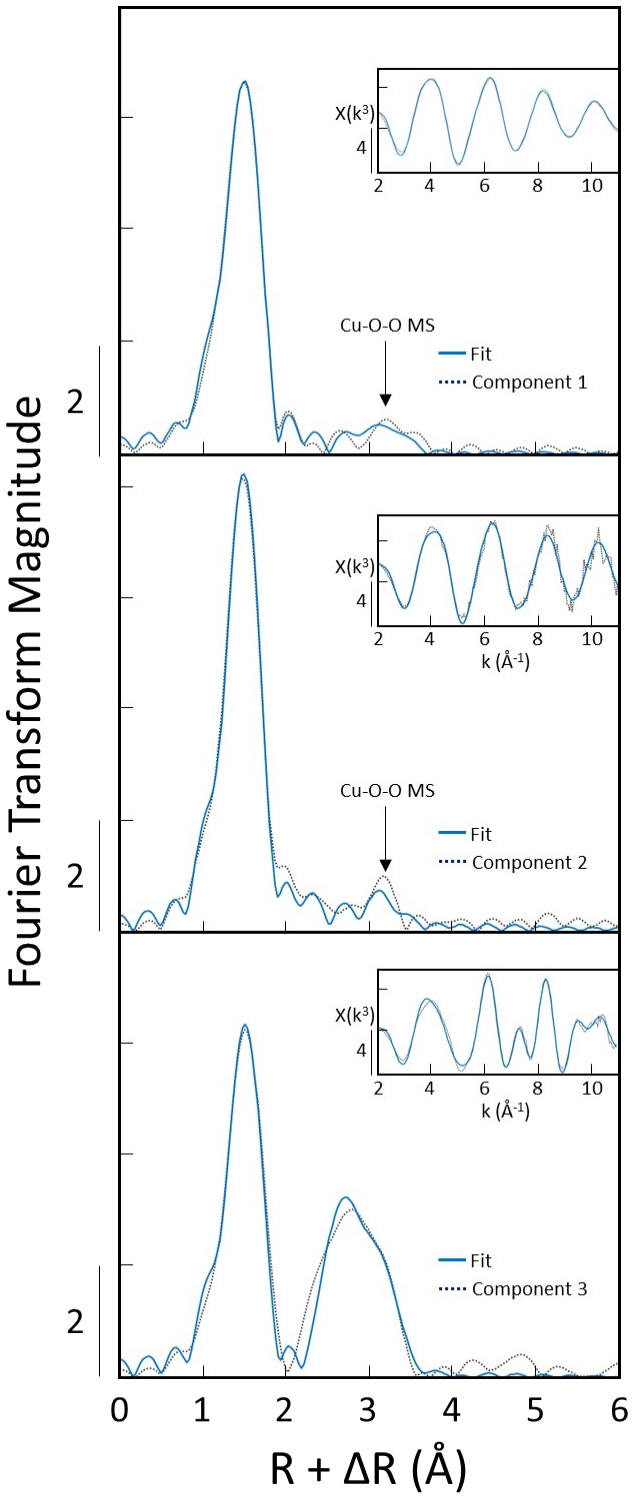

Figure S7: Output of the shell-by-shell fits (blue lines) overlain on ITFA-extracted principal components; Component 1 (top panel), Component 2 (middle panel) and Component 3 (bottom panel). The inset in each panel shows the corresponding EXAFS spectra. Components 1, 2 and 3 are interpreted as outer-sphere Cu complexes, inner-sphere Cu complexes and polymeric Cu, respectively.

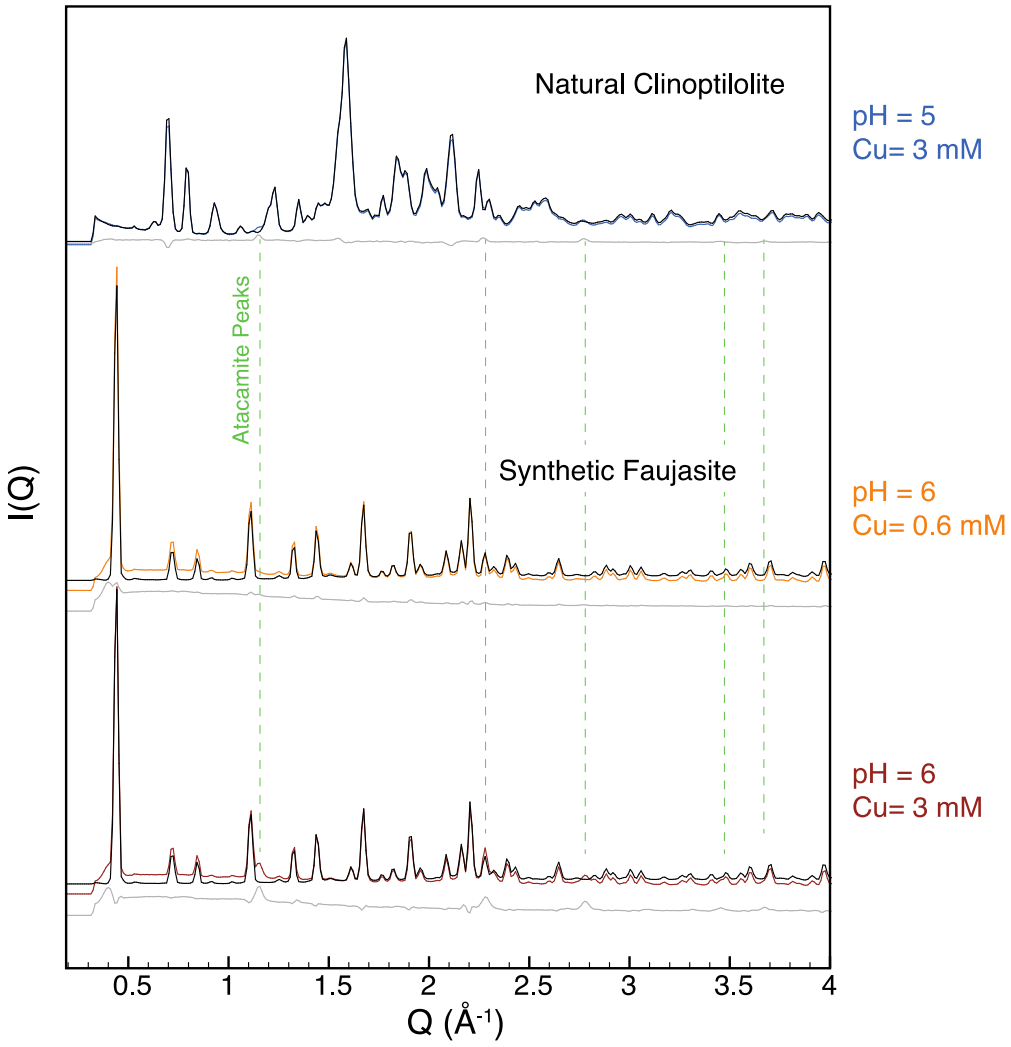

Figure S8: Synchrotron XRD data of natural clinoptilolite (top) without Cu exposure (black) and after exposure to 3 mM Cu at pH 5 (blue), synthetic faujasite (middle) without Cu exposure (black) and after exposure to 0.6 mM Cu at pH 6 (orange) and synthetic faujasite (bottom) without Cu exposure (black) and after exposure to 3 mM Cu at pH 6 (brown). Peak positions for atacamite are indicated by green dashed lines. Differences between reacted and unreacted samples are given in grey.

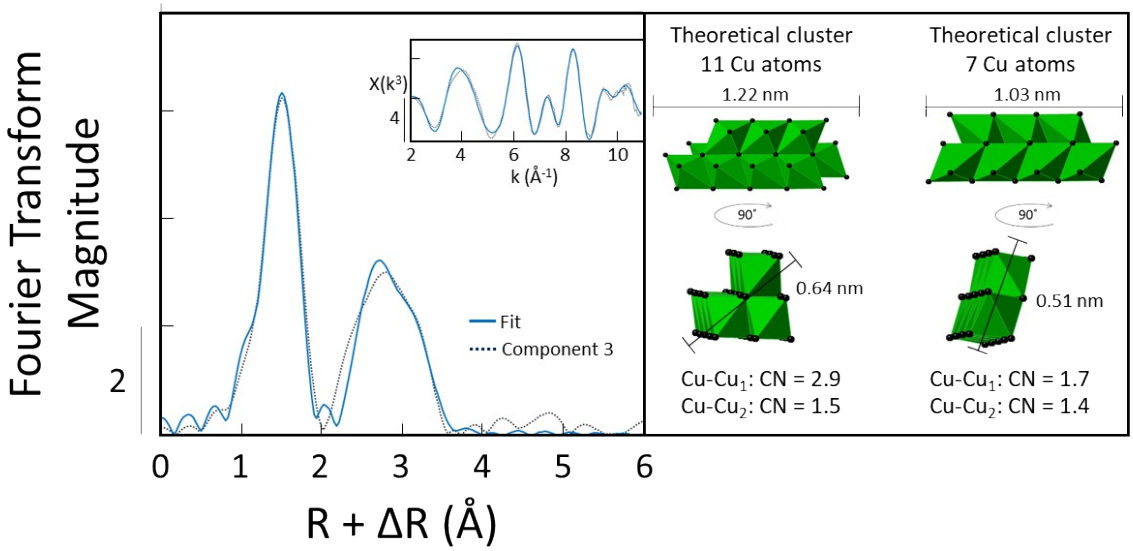

188

189 Figure S9: Models of polymeric Cu-Cu clusters derived from EXAFS shell-by-shell fits of
190 Component 3. The fit-derived coordination number (CN) for the Cu-Cu_1 and Cu-Cu_2 atomic
191 pairs was 1.9±0.3 and 1.4±0.3 (Table S3).

192

193

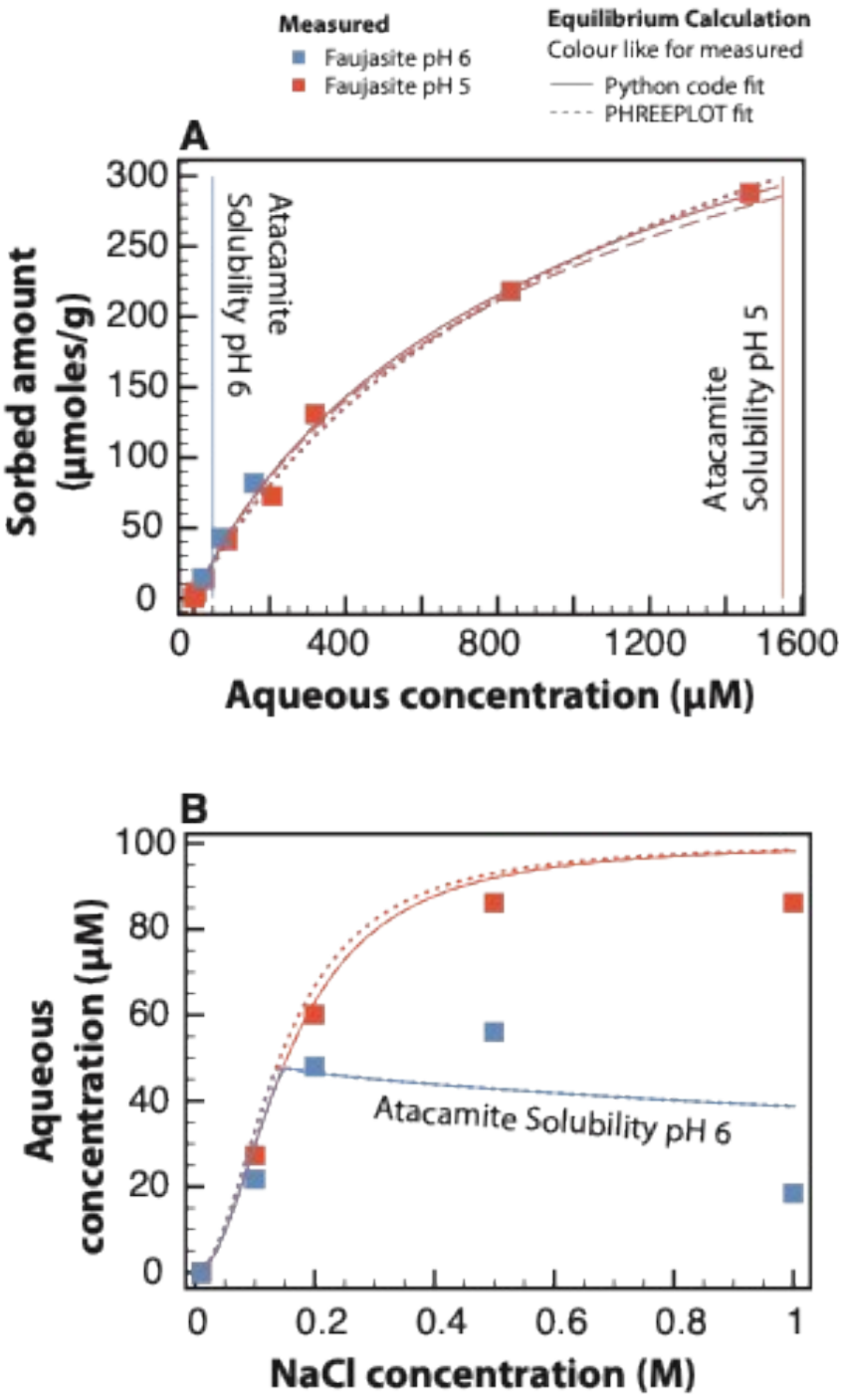

194

195 Figure S10: Adsorption isotherms at 25 °C for A) Cu(II) uptake by synthetic faujasite at pH 5
196 and 6, B) Measured and calculated Cu concentration resulting from uptake by synthetic
197 faujasite as a function of NaCl concentration. The decrease in the calculated aqueous
198 concentration at pH 6 and elevated NaCl concentration reflects atacamite precipitation. Initial
199 aqueous Cu(II) concentration was 0.1 mM.

Table S1. Reactions and equilibrium constants for speciation and solids use in the Cu system

Reaction	**log K**	**Source**
$Cu^{2+} + OH^- = CuOH^+$	-7.96	Haung (1989)
$Cu^{2+} + 2OH^- = Cu(OH)_2$	-16.23	Haung (1989)
$Cu^{2+} + Cl^- = CuCl^+$	0.11	Haung (1989)
$Cu^{2+} + 2Cl^- = CuCl_2$	0	Haung (1989)
$Cu^{2+} + 3Cl^- = CuCl_3^-$	-1	Haung (1989)
$Cu^{2+} + 4Cl^- = CuCl_4^{2-}$	-3.7	Adjusted
Atacamite solubility		
$Cu_2(OH)_3Cl + 3H^+ = 2Cu^{2+} + 3H_2O + Cl^-$	7.34	MINTEQ

200

202 Table S2. Pitzer parameters used in the simulations.

Parameter	Species 1	Species 2	Species 3	Value
b^0	Cu^{2+}	Cl^-		0.448214
	$CuCl_3^-$	Cu^{2+}		0.005214
	$CuCl_4^{2-}$	Cu^{2+}		0.793398
	$CuCl^+$	Cl^-		0.08247
	$CuCl_3^-$	$CuCl^+$		0.601236
	$CuCl_4^{2-}$	$CuCl^+$		0.297845
	$CuCl_3^-$	Na^+		0.151208
	$CuCl_4^{2-}$	Na^+		-0.006297
b^1	Cu^{2+}	Cl^-		1.31604
	$CuCl_3^-$	Cu^{2+}		-0.352932
	$CuCl_4^{2-}$	Cu^{2+}		1.520066
	Cl^-	$CuCl^+$		0.147128
	$CuCl_3^-$	$CuCl^+$		0.147128
	$CuCl_4^{2-}$	$CuCl^+$		0.43696
	$CuCl_3^-$	Na^+		0.040213
	$CuCl_4^{2-}$	Na^+		0.0505922
b^2	$CuCl_4^{2-}$	Cu^{2+}		2.528826
C^f	Cu^{2+}	Cl^-		0.001663
	$CuCl_3^-$	Cu^{2+}		0.351581
	$CuCl_4^{2-}$	Cu^{2+}		0.293231
	$CuCl_3^-$	$CuCl^+$		0.700384
	$CuCl_4^{2-}$	$CuCl^+$		0.340713
	$CuCl_3^-$	Na^+		-0.012021
	$CuCl_4^{2-}$	Na^+		0.004219
θ	$CuCl^+$	Cu^{2+}		-0.016065
	$CuCl_3^-$	Cl^-		0.078296
	$CuCl_4^{2-}$	Cl^-		0.25659
	$CuCl_3^-$	$CuCl_4^{2-}$		0.326518
	Cu^{2+}	Na^+		0.01966
	$CuCl^+$	Na^+		-0.013918
l	$CuCl_2$	$CuCl^+$		0.416289
	$CuCl_2$	Cu^{2+}		0.469588
	$CuCl_2$	$CuCl_3^-$		1.521582
	$CuCl_2$	$CuCl_4^{2-}$		0.273556
	$CuCl_2$	Cl^-		0.080942
	$CuCl_2$	Na^+		0.041578
y	Cu^{2+}	$CuCl^+$	Cl^-	0.045495
	Cu^{2+}	$CuCl^+$	$CuCl_3^-$	-0.002276
	Cu^{2+}	$CuCl^+$	$CuCl_4^{2-}$	0.171585
	Cu^{2+}	Cl^-	$CuCl_3^-$	0.52963
	Cu^{2+}	Cl^-	$CuCl_4^{2-}$	0.230288
	Cu^{2+}	$CuCl_3^-$	$CuCl_4^{2-}$	-4.991511
	$CuCl^+$	Cl^-	$CuCl_3^-$	0.656652
	$CuCl^+$	Cl^-	$CuCl_4^{2-}$	0.151079
	$CuCl^+$	$CuCl_3^-$	$CuCl_4^{2-}$	-3.988599
	Cu^{2+}	Na^+	Cl^-	0.02153
	$CuCl^+$	Na^+	Cl^-	-0.009949
	Cu^{2+}	Na^+	$CuCl_3^-$	-0.34397
	$CuCl^+$	Na^+	$CuCl_3^-$	3.20739
	Cu^{2+}	Na^+	$CuCl_4^{2-}$	0.001007
	$CuCl^+$	Na^+	$CuCl_4^{2-}$	-0.020676
	Cl^-	$CuCl_3^-$	Na^+	0.008721
	$CuCl_3^-$	$CuCl_4^{2-}$	Na^+	-0.002515

203 Parameter values were adopted from Haung (1989) except for the $CuCl^+$ - Cl^- interaction,
204 which was omitted after tests

Table S3: Cu K-edge shell-by-shell fitting results

Sample Name	Atomic Pairs	CN	R (Å)	σ^2 (Å^2)	ΔE_0 (eV)	R-Factor
CuO[A]	Cu-O	3.2 (0.4)	1.96 (0.01)	0.002 (0.001)	1.0 (1.5)	0.009
	Cu-Cu1	5.8 (0.9)	2.92 (0.01)	0.007		
	Cu-Cu2	5.3 (1.1)	3.13 (0.01)	0.006		
	Cu-Cu3	4.2 (0.9)	3.43 (0.01)	0.006		
	Cu-O-O	8	3.94 (0.08)	0.007		
Aqueous Cu(II)	Cu-O	4.3 (0.2)	1.97 (0.01)	0.007 (0.001)	-3.2 (0.6)	0.007
	Cu-O-O	8	4.04 (0.03)	0.007		
Comp. 1	Cu-O	4.3 (0.2)	1.97 (0.01)	0.007 (0.001)	-3.2 (0.6)	0.007
	Cu-O-O	8	4.04 (0.03)	0.007		
Comp. 2	Cu-O	3.8 (0.3)	1.94 (0.01)	0.004 (0.001)	-1.7 (1.2)	0.018
	Cu-Si/Al	0.8 (0.5)	2.82 (0.05)	0.012		
	Cu-O-O	8	3.96 (0.05)	0.007		
Comp. 3	Cu-O	3.5 (0.4)	1.97 (0.01)	0.006 (0.001)	-2.4 (1.3)	0.015
	Cu-Cu1	1.9 (0.3)	3.04 (0.01)	0.007		
	Cu-Cu2	1.4 (0.3)	3.45 (0.01)	0.006		
	Cu-O-O	8	3.99 (0.05)	0.007		

[A]The fits of CuO were modelled after those described in (Cheah et al., 2000) The constrained σ^2 values in the CuO fits and the CN of the Cu-O-O MS path were taken from Cheah et al. 2000. For all fits, fitting parameters that were allowed to float are accompanied by fit determined standard errors in parenthesis, whereas constrained parameters are written without parentheses. The number of independent points was 17.0 for all fits, whereas the number of variables ranged from was 5 to 11. The first were performed from 1-4 Å and S_0^2 was constrained to 0.9.

214 Table S4. Fitted values for exchange reaction constant (logarithmic) and CEC.

Zeolite	Method	System	Log K_{Cu}	Log K_{Pb}	CEC (mmoles/g)
Synthetic faujasite	PHREEPLOT	Cu	0.878		1.38
	Python App	Cu	0.856		1.44

215

216
217

References

Allison, J.D., Brown, D.S., Novo-Gradac, K.J., 1990. MINTEQA2/PRODEFA2—A Geochemical Assessment Model for Environmental Systems: Version 3.0 User's Manual. U.S. Environmental Protection Agency, Athens, Georgia.

Belokoneva, E.L., Gubina, Y.K., Forsyth, J.B., Brown, P.J., 2002. The charge-density distribution, its multipole refinement and the antiferromagnetic structure of dioptase, Cu6[Si6O18]·6H2O. Phys. Chem. Miner. 29, 430–438. https://doi.org/10.1007/s00269-002-0246-6

Cheah, S.F., Brown, G.E., Parks, G.A., 2000. XAFS study of Cu model compounds and Cu2+ sorption products on amorphous SiO2, γ-Al2O3, and anatase. Am. Mineral. 85, 118–132. https://doi.org/10.2138/am-2000-0113

Downes, C.J., Pitzer K.S., 1976. Thermodynamics of electrolytes. Binary mixtures formed from aqueous NaCl, Na_2SO_4, $CuCl_2$, and $CuSO_4$ at 25°C. J. Solut. Chem. 5, 389-398.

Haung, H.-H. (1989) Estimation of Pitzer's ion interaction parameters for electrolytes involved in complex formation using a chemical equilibrium model. J. Solut. Chem. 18, 1069-1084.

Kim, H.-T., Frederick Jr., W.J., 1988. Evaluation of Pitzer Ion Interaction Parameters of Aqueous Electrolytes at 25 °C: 1. Single Salt Parameters. J. Chem. Eng. Data 33, 177-184.

Ma, X.-C., Li, X.-P., He, X.-F., Sang, S.-H., Lei, N.-F., Nie, Z., 2019. Thermodynamic Study of the NaCl−$CuCl_2$−H_2O Ternary System at 298.15 K by the Electromotive Force Method. J. Chem. Eng. Data 64, 90−97.

Le Roux, S. G., Miller, J. A., Dunford, A. J. and Clarke, C. E. (2016) The dissolution kinetics of atacamite in the acid range and the stability of atacamite. Appl. Geochem. 64, 22-29.

Moog, H. C. and Cannepin, R. (2014) Entwicklung von thermodynamischen Daten für die Belange der thermodynamischen Gleichgewichtsmodellierungvon Prozessen in tiefen, geothermalen Schichten. In: Teilprojekt A (GRS): Bestimmung von Ionenwechselwirkungskoeffizienten und Aufstellung eines Reservoirmodells. 165 pp. Available at https://www.grs.de/sites/default/files/pdf/grs-337.pdf

Newville, M., 2001. IFEFFIT: interactive XAFS analysis and FEFF fitting. J. Synchrotron Radiat. 322–324. https://doi.org/https://doi.org/10.1107/S0909049500016964

Oswald, H.R., Reller, A., Schmalle, H.W., Dubler, E., 1990. Structure of copper(II) hydroxide, Cu(OH)2. Acta Crystallogr. Sect. C Cryst. Struct. Commun. 46, 2279–2284. https://doi.org/10.1107/s0108270190006230

Rehr, J.J., Albers, R.C., Zabinsky, S.I., 1992. High-order multiple-scattering calculations of X-ray absorption fine structure. Phys. Rev. Lett. 3397–3400.

Sushkevich, V.L., Safonova, O. V., Palagin, D., Newton, M.A., van Bokhoven, J.A., 2020. Structure of copper sites in zeolites examined by Fourier and wavelet transform analysis of EXAFS. Chem. Sci. 11, 5299–5312. https://doi.org/10.1039/d0sc01472a

Vital, M., Pedersen, T.v.B., Molander, J., Jakobsen, R., Tobler, D.J., Dideriksen, K., 2025. Dissolution kinetics for the Fe(II)-Fe(III) layered double hydroxide, green rust. Appl. Clay

Sci. 272, 107814. Fitting routine available at ; available at
https://geusgitlab.geus.dk/geochemical-modelling/fitting-phreeqc